Indian Journal of Pure & Applied Physics
Vol. 64, May 2026, pp. 555-565
DOI: 10.56042/ijpap.v65i5.28363

Theoretical Investigation and Design Optimization of a Metamaterial Enhanced THz Detector for Room Temperature Terahertz Imaging

Garishma Kalra[a], Khushbu Singh Raghav[a], Deepak Bansal[a,b] & Amit Kumar[a,b*]

[a]CSIR-Central Electronics Engineering Research Institute, Pilani, Rajasthan 333 031 India
[b]Academy of Scientific and Innovative Research (AcSIR), Ghaziabad 201 002, India

Received: 6th February 2026; accepted: 5th March 2026

This paper presents the theoretical investigation, finite-element simulation, and design optimization of a Metamaterial-Enhanced THz Detector for Room-Temperature Terahertz Imaging. The proposed detector consists of a suspended MEMS platform incorporating a 3×3 array of square-patch MMA unit cells optimized for imaging at 1 THz. Electromagnetic simulations demonstrate polarization-insensitive absorbance exceeding 80 % at the target frequency, with stable performance for incidence angles up to 45°. The suspended platform is supported by Au–SiO_2 bimorph actuators engineered to balance sensitivity and response speed. An analytical model is developed to investigate and identify a trade-off among different performance parameters. For an optimized platform area of 230 µm × 230 µm and a dielectric thickness of 1.5 µm, the detector achieves a designed time constant of 300 ms with 253 µm-long bimorph actuators and 0.8 fractional Au coverage. Finite-element simulations in CoventorWare® validate the analytical predictions, yielding a thermomechanical sensitivity of 0.063°/K and a responsivity of 0.056°/µW, with a temperature rise of 1.25 K under 1 µW incident power. Noise analysis indicates that temperature-fluctuation noise dominates, yielding a noise-equivalent power (NEP) of 2 pW at 295 K. The proposed analytical design methodology provides a method for developing high-sensitivity, room-temperature detectors suitable for THz imaging.

Keywords:THz detector, Metamaterial absorber, THz imaging, THz absorption

1 Introduction

Terahertz radiation in the 0.1–10 THz frequency range has garnered substantial interest due to its wide-ranging applications in biomedical imaging[1], security surveillance[2], pharmaceutical quality control[3], and high-speed wireless communication[4]. Among the essential components of a THz system, the detector is particularly critical, as its performance directly influences overall system capability and practical implementation. THz detectors are broadly categorized into photon detectors[5] and thermal detectors[5] based on their detection mechanisms. Photon detectors generate photocurrent by exciting charge carriers upon THz absorption. In contrast, thermal detectors respond by producing a temperature rise, which is subsequently measured via a temperature-sensitive element. While photon-based detectors such as photoconductors, Schottky barrier diodes, and superconducting tunnel junction detectors typically provide high sensitivity and fast response times, they often require cryogenic cooling, which increases cost, complexity, and power consumption, thereby limiting their practicality in many real-world applications.

Thermal detectors such as Golay cells[6] and pyroelectric detectors[7] generally exhibit slower response; however, they operate at room temperature with satisfactory sensitivity. Raster scanning to acquire an image and reconstruct a 2-D image requires long acquisition times with such single-pixel elements, thereby limiting its suitability for real-time imaging applications. Large array detectors with micromachining capability are thus required for simultaneous data acquisition and image construction. Efforts have been made to use IR microbolometers for THz imaging[8]; however, they suffer from poor sensitivity due to inefficient THz absorption, the absence of THz absorbers, and optical cavities optimized for IR wavelengths[9].

Metamaterial absorber (MMA) comprising periodic subwavelength elements that can be geometrically tailored to achieve strong THz absorption at targeted frequencies[10,11]. Researchers have explored different configurations of metamaterials, including closed-ring[12], Split-ring[13], cut-wire[14] and MEMS

*Corresponding author: E mail:amitkumar.ceeri@csir.res.in

resonators[15]; however, these suffer from polarization sensitivity. Efforts have been made to develop MMAs with a symmetric geometrical configuration and polarization-independent behaviour[16,17]. When incorporated onto MEMS platforms, absorbed radiation is converted into heat, causing deflection of the supporting bimorph actuators, which can be accurately monitored using optical methods[18,19]. Bimorph-based platforms have been extensively studied for IR detection[20] and have recently emerged as attractive candidates for THz sensing[21]. Although previous works have demonstrated the fabrication and characterization of MMA-integrated THz detectors[22,23], a comprehensive analytical model with simulation validation has received insufficient attention in the literature.

This paper presents the theoretical investigation of a bimorph-based THz detector for room-temperature THz imaging. The novelty of this work lies in the development of a comprehensive analytical design methodology for a MEMS THz detector that captures its coupled EM, thermal, and mechanical behaviour. Unlike prior studies that primarily focused on absorber optimization and experimental validation, the proposed approach establishes analytical relationships among thermal capacitance, conductance, thermomechanical sensitivity, responsivity, and response time. The introduction of Au fractional coverage in the bimorph actuator as a controllable design parameter provides an effective mechanism for tuning the sensitivity–speed trade-off without altering the thickness or composition of the constituent layers. In addition, the integration of a polarization-insensitive 3×3 square-patch MMA with greater than 80% absorption at 1 THz and angular stability up to 45° ensures efficient THz-to-heat conversion. The selection of 1 THz frequency for detector design is based on several factors, including atmospheric attenuation, spatial resolution, penetration depth, and fabrication compatibility. The targeted frequency lies within a relatively low-attenuation window, offering good spatial resolution due to the small wavelength of 300 µm. This offers an excellent opportunity for high-resolution imaging compared to lower THz frequencies (0.1–0.5 THz) while maintaining sufficient penetration depth. From a fabrication-compatibility perspective, the targeted frequency yields a patch size of 70 µm and an inter-patch gap of 5 µm, easily possible with standard MEMS fabrication technology. The optimized thermomechanical sensitivity of 0.063°/K and responsivity of 0.056°/µW, with a response time of 300 ms and a NEP of 2 pW, are comparable to or better than those of similar designs reported in the literature. The close agreement between the analytical model and finite-element simulations further validates the design approach and provides a scalable method for developing MEMS detectors that operate across different frequency bands.

2 Materials and Methods

2.1 Terahertz Detector

The 3-D model of the proposed MEMS THz detector is shown in Fig. 1. The structure consists of a suspended MEMS platform supported by two symmetrically arranged bimorph actuators composed of materials exhibiting a large difference in their coefficients of thermal expansion (α). The suspended platform is integrated with a metamaterial absorber comprising a dielectric layer sandwiched between a periodic array of square metallic patches and a continuous metallic ground layer.

When THz radiation with power P_o incident on the MMA, resonant electromagnetic modes are excited within the structure. The electric dipole resonance due to charge accumulation on the metallic patches, and magnetic dipole resonance due to antiparallel surface currents on the top and the ground metal layer, enhance impedance matching and promote strong resonant absorption of the incident radiation, leading to an increase in the temperature (ΔT), which is given by

$$C\frac{d(\Delta T)}{dT}+G\Delta T=P_0 \qquad \ldots(1)$$

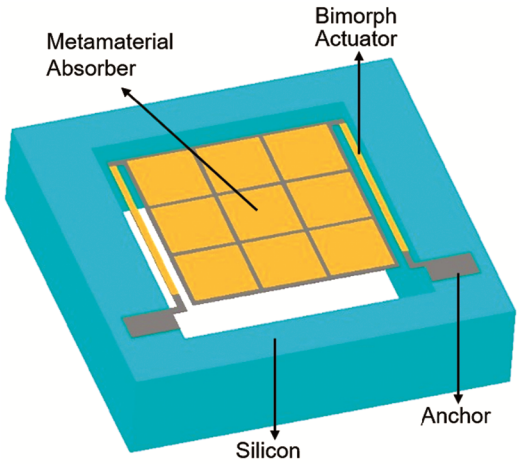

Fig. 1 — 3D model of the proposed THz detector

where C is the thermal capacitance of the multilayer platform, and G is the thermal conductance of the structure. The thermal capacitance depends on the density (ρ) and specific heat (C_{th}) of the constituent layers and is given by

$$C = \sum C_{th} \cdot \rho \cdot A \cdot t \quad \ldots(2)$$

where A and t denote the area and thickness of the constituent layers, respectively. The generated heat is primarily dissipated to the surroundings via conduction along the bimorph actuators. Heat losses due to convection and radiation are considered negligible, as the detector is desired to be operated under vacuum conditions and at relatively low temperatures. In practical implementation, vacuum conditions to minimize convection losses can be achieved through wafer-level hermetic encapsulation technique, which is widely employed in MEMS fabrication and packaging[24]. The steady-state temperature rise of the platform is obtained by solving Eq. 1 and is given by[25]

$$\Delta T(t) = \frac{\eta P_0}{G\sqrt{1+\tau^2}} \quad \ldots(3)$$

where η denotes the absorbance of the MMA layer. τ is the thermal time constant defined as the time required for the detector to reach a steady state after radiation exposure. A lower thermal conductance enhances heat confinement, producing a larger temperature gradient across the bimorph actuators and consequently a greater angular deflection (θ) at the free end. The primary performance metrics of the proposed THz detector are the thermomechanical sensitivity ($d\theta/dT$) and the responsivity (R), and are given by[26]

$$\frac{d\theta}{dT} = 6L(\alpha_1 - \alpha_2) \cdot \frac{(t_1 + t_2)}{t_2^2\left(4 + 6\frac{t_1}{t_2} + 4\frac{t_1^2}{t_2^2} + \frac{E_1}{E_2}\frac{t_1^3}{t_2^3} + \frac{E_2}{E_1}\frac{t_2}{t_1}\right)} \quad \ldots(4)$$

$$R = \frac{d\theta}{dP} = \frac{\eta}{G\sqrt{1+\omega^2\tau^2}}\frac{d\theta}{dT} \quad \ldots(5)$$

where E and t are the Young's modulus and thicknesses of the constituent layers of the bimorph actuator. The incident radiation is modulated at a frequency ω and is absorbed by the MMA with an absorption efficiency η. Although reducing the thermal conductance of the actuators enhances heat confinement, thereby increasing temperature, sensitivity, and responsivity, it negatively affects the detector's dynamic performance. Specifically, a lower thermal conductance increases the thermal time constant, which is given by[26]

$$\tau = \frac{C}{G} \quad \ldots(6)$$

Equations (4)–(6) indicates that detector sensitivity (or responsivity) and response time are competing parameters. Hence, an optimal balance between sensitivity and speed must be established to achieve the desired overall performance. The proposed THz detector is therefore developed through a structured design approach consisting of three key stages: (a) the design of a polarization-insensitive, high absorbance MMA at 1 THz; (b) the design of bimorph actuators to achieve a targeted response time of 300 ms; and (c) the simulation and optimization of the integrated THz detector, incorporating both the MMA and the bimorph actuator, to evaluate its thermomechanical sensitivity, responsivity, and noise performance. The detailed design methodology for each component is described in the following sections.

2.2 Metamaterial Absorber (MMA) Design

The three-layered metamaterial absorber, consisting of a periodic array of metal patches deposited on a highly absorptive dielectric and backed by a metal ground layer, is shown in Fig. 2.

When THz radiation impinges on the metamaterial absorber, charges of opposite polarity are deposited at the two ends of the top metal patches. The strong electromagnetic coupling induces opposite charges on the ground layer, leading to currents flowing in opposite directions on the top and ground layers, as shown in Fig. 3 (a). The accumulation of charges on

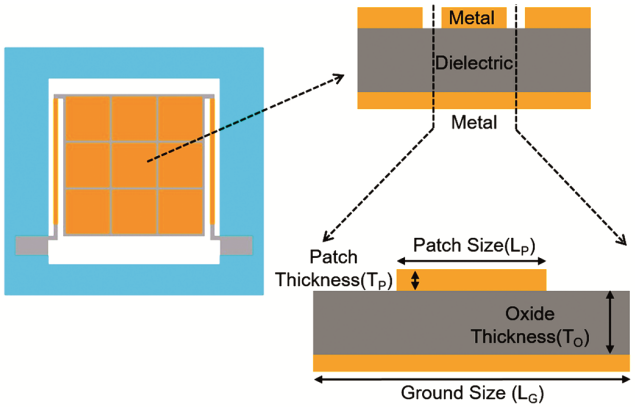

Fig. 2 — Top view and cross-section of metamaterial absorber

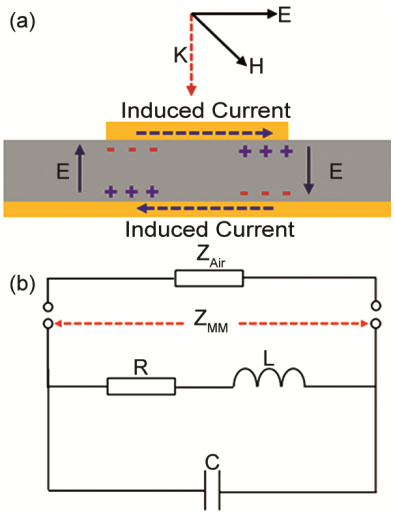

Fig. 3 — (a) Induced charge and current distribution in MMA; and (b)Equivalent RLC model

the two metal patches forms electric dipoles, leading to electric dipole resonance. Meanwhile, antiparallel currents flowing through the two metal patches generate magnetic dipoles, producing magnetic dipole resonance within the dielectric layer. The combined presence of these two resonances facilitates resonant absorption of incident THz radiation, whose behaviour can be modelled by an RLC circuit[27], as shown in Fig. 3 (b). The charges induced by the incident electromagnetic field are modelled as a capacitor C; a resistor R represents the power dissipated in the dielectric layer; and the oscillating current in the metal patch and ground layer is modelled as an inductor L.

The equivalent impedance of the metamaterial absorber (Z_{MM}) and impedance of the free space at the metamaterial-air interface (Z_{Air}) are given by[27]

$$Z_{MM} = \frac{R + j\omega L}{1 - \omega^2 LC + j\omega RC} \quad \ldots(7)$$

$$Z_{Air} = \sqrt{\mu_o / \varepsilon_o} = 120\pi\Omega \quad \ldots(8)$$

Upon irradiation, a portion of the incident THz radiationis reflected due to impedance mismatch at the metamaterial-air interface. A portion of the accepted radiation is transmitted through the ground plane, and the remainder is absorbed by the dielectric layer. The absorbance *A(w)* is given by

$$A(w) = 1 - R(w) - T(w) \quad \ldots(9)$$

where *R(w)* and *T(w)* are the reflectance and transmittance of the metamaterial absorber. These parameters can be extracted by representing the metamaterial absorber as a two-port network, wherein the reflectance and transmittance are given by

$$R(w) = |S_{11}|^2 \quad \ldots(10)$$

$$T(w) = |S_{21}|^2 \quad \ldots(11)$$

The thickness of the ground layer is kept greater than the skin depth at the operating frequency to suppress transmission (S_{21}=0). The geometry and dimensions of the metal patch, the spacing between patches, and the thickness of the dielectric layer determine Z_{MM}, which must be optimized to achieve perfect impedance matching at the upper interface, i.e., Z_{MM}=Z_{Air}. The trade-off between perfect absorption and detection speed is achieved by judiciously selecting the absorber thickness, as thick dielectric layers increase absorption but also thermal capacitance. The absorption efficiency in such a case is given by

$$\eta = 1 - |S_{11}|^2 \quad \ldots(12)$$

The scattering parameters and absorption characteristics of MMA are analyzed using finite-element simulation in Ansys Electronic Desktop. To minimize computational cost and simulation time, a single unit cell is analyzed rather than a large array, with master–slave boundary conditions and Floquet port excitation. The unit cell consists of a square patch of size L_P and thickness T_P separated from a metal ground by a dielectric layer of thickness T_0. Gold (Au) is selected for both the top and bottom metal layers, and silicon dioxide (SiO_2) with a complex dielectric constant of 3.99-0.1i is selected as the dielectric absorber. The thicknesses of both the top metallic patch and the ground plane are fixed at 200 nm. The patch size is optimized by fixing the silicon dioxide thickness at 1.5 µm and varying the patch size from 65 µm to 75 µm with a patch separation of 5 µm. The peak absorbance vs resonant frequency for different patch sizes is shown in Fig. 4.

The results show a linear decrease in resonance frequency with increasing patch size, with a resonance centered at 1 THz achieved for a patch dimension of 70 µm. To further optimize absorber performance, the effect of the dielectric thickness is investigated while maintaining a patch size of 70 µm and an inter-patch gap of 5 µm, with the SiO_2 thickness varying from 1 µm to 2 µm. The analysis

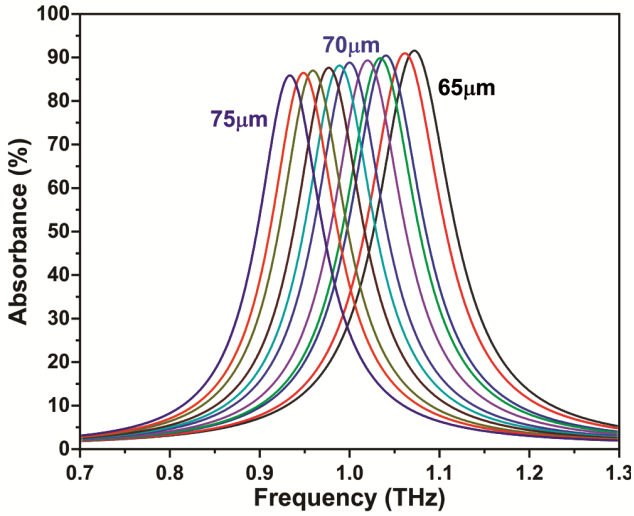

Fig. 4 — Absorbance vs Frequency for different patch dimensions

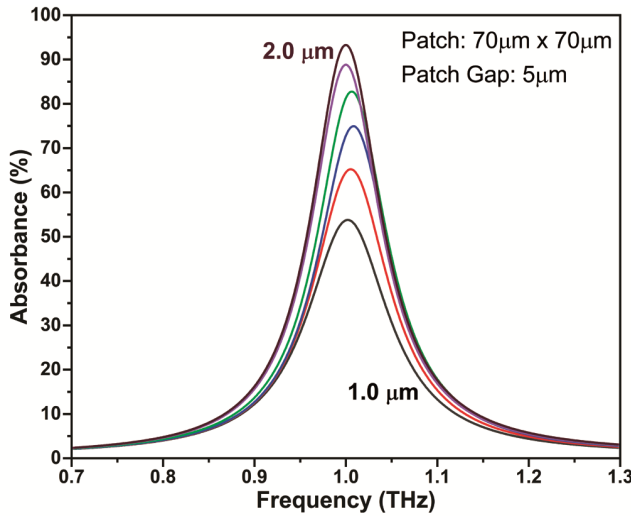

Fig. 5 — Absorbance vs Frequency for different dielectric thicknesses

indicates that a dielectric thickness of 1.5 μm results in absorption exceeding 80 % at the 1 THz, as shown in Fig. 5.

The absorbance characteristics of MMA under different polarizations and incidence angles are analyzed to assess polarization insensitivity and angular stability. The result shows that the MMA exhibits excellent insensitivity to polarization angle, as shown in Fig. 6 (a) for an incident wave normal to the MMA surface. The absorption spectra for TE- and TM-polarized waves at different incidence angles are shown in Fig. 6 (b). The result shows that the absorbance remains above 80 % for $\theta < 45°$, indicating good incident-angle stability. The optimized MMA provides the foundation for

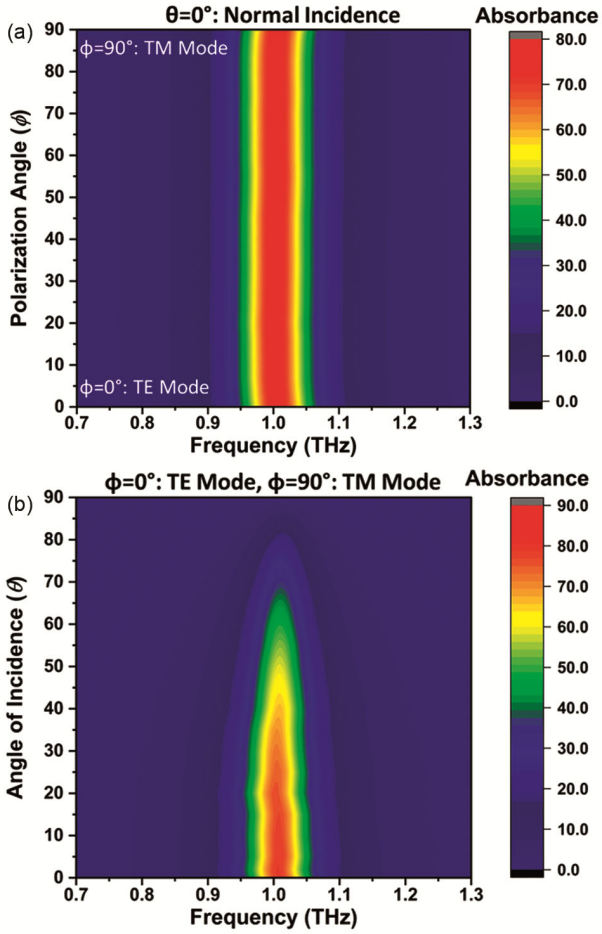

Fig. 6 — Absorbance spectra for (a) Different polarization angles; and (b) Different angles of incidences (θ)

subsequent thermo-mechanical modelling of the MEMS platform, including the design of the bimorph actuator, as it directly influences the temperature, responsivity, speed, and overall response of the proposed THz detector.

2.3 Bimorph Actuator Design

The MMA serves as the heat source for actuating the bimorph structure. Under THz irradiation, absorbed energy increases the temperature, generating differential thermal expansion between the bimorph layers and inducing mechanical deflection. Increasing the absorber area increases the thermal capacitance; maintaining a constant response time, therefore, requires a proportional increase in thermal conductance, typically achieved by shortening the bimorph. However, since the temperature rise scales inversely with thermal conductance, enhanced heat dissipation reduces the steady-state temperature rise, thereby diminishing thermomechanical deflection and responsivity.

The proposed bimorph consists of Au and SiO_2 layers with thicknesses similar to those of the MMA, facilitating a simplified design. While the maximum deflection occurs when the layer thicknesses of the SiO_2 and Au layers are nearly equal (As E for SiO_2=68 GPa and Au=77 GPa), the current choice of thickness is a deliberate trade-off between thermomechanical sensitivity, thermal conductance, response time and responsivity. Using a bimorph with a thickness similar to that of the absorber layer significantly reduces fabrication complexity by avoiding additional deposition, lithography and etching steps. The thermomechanical performance is determined by thermal conductance and structural stiffness, which ultimately govern detector sensitivity and response speed. With fixed layer thicknesses, the thermal conductance can be modulated only by varying the bimorph width, length and fractional coverage of the Au layer.

The cross-section of the bimorph actuator is shown in Fig. 7. The structure consists of a fractional coverage x (where $0 < x < 1$) of the SiO_2 layer covered by an Au layer, while the remaining fraction $1-x$ comprises the SiO_2 layer only. The effective thermal conductance of the bimorph can be modelled by considering two distinct sections: (i) the Au–SiO_2 composite section of length $x \cdot L_{Leg}$, and (ii) the SiO_2-only section of length $(1-x) \cdot L_{Leg}$. Since heat flows along the length of the bimorph, and the Au and SiO_2 layers in the composite section are stacked vertically, they act as parallel thermal paths.

The thermal conductance of the Au-SiO_2 section of length $x \cdot L_{Leg}$ is given by

$$G_{Au-SiO_2} = \left(\frac{g_{Au} \cdot A_{Au}}{x \cdot L_{Leg}} \right) + \left(\frac{g_{SiO_2} \cdot A_{SiO_2}}{x \cdot L_{Leg}} \right) \quad \ldots(13)$$

The thermal conductance of the SiO_2 section of length $(1-x) \cdot L_{Leg}$ is given by

$$G_{SiO_2} = \frac{g_{SiO_2} \cdot A_{SiO_2}}{(1-x) \cdot L_{Leg}} \quad \ldots(14)$$

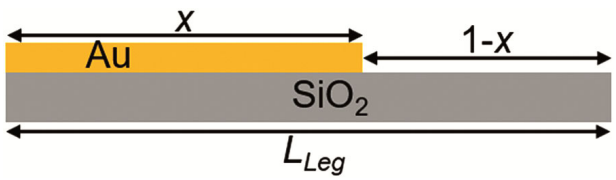

Fig. 7 — Cross-section of bimorph actuator with Au fractional coverage (x)

where g_i is the thermal conductivity, and A_i is the cross-sectional area of the constituent layers. Since these two sections are connected in series along the direction of heat flow, the overall effective thermal conductance of the bimorph actuator is given by

$$\frac{1}{G_{Leg}} = \frac{1}{G_{Au-SiO_2}} + \frac{1}{G_{SiO_2}} \quad \ldots(15)$$

Rearranging the terms, the effective thermal conductance is given by

$$G_{Leg} = \frac{(g_{Au} \cdot A_{Au} + g_{SiO_2} \cdot A_{SiO_2})(g_{SiO_2} \cdot A_{SiO_2})}{L_{Leg}((1-x) \cdot g_{Au} \cdot A_{Au} + g_{SiO_2} \cdot A_{SiO_2})} \quad \ldots(16)$$

The bimorph length (L_{leg}) as a function of thermal capacitance, thermal conductance, actuator geometry, response time and material properties is obtained by rearranging Eqs. 2, 6 and 13 and is given by

$$L_{Leg} = \frac{\tau(g_{Au} \cdot A_{Au} + g_{SiO_2} \cdot A_{SiO_2})(g_{SiO_2} \cdot A_{SiO_2})}{(\sum C_{th} \cdot \rho \cdot A \cdot t) \cdot ((1-x) \cdot g_{Au} \cdot A_{Au} + g_{SiO_2} \cdot A_{SiO_2})} \quad \ldots(17)$$

The lengths of the Au-SiO_2 section and the SiO_2 section of the bimorph actuator are given by

$$L_{Au-SiO_2} = x \cdot L_{Leg} \quad \ldots(18)$$

$$L_{SiO_2} = (1-x) \cdot L_{Leg} \quad \ldots(19)$$

The material properties of the different structural layers considered in the analytical modelling and finite element simulation are given in Table 1.

The required bimorph length for an optimized MMA with a 230 µm × 230 µm active area and 1.5 µm dielectric thickness is shown in Fig. 8 for various response times. The cantilever width is fixed

Table 1 — Material properties of different structural layers

Layers	Au	SiO_2
Thermal conductivity (g) ($Wm^{-1}K^{-1}$)	296	1.4
Specific heat (c) ($J\ Kg^{-1}\ K^{-1}$)	129	703
Density (ρ) ($Kg\ m^{-3}$)	19300	2200
Young's Modulus (E) (GPa)	77	68
Coefficient of Thermal Expansion (α) ($\times 10^{-6}\ K^{-1}$)	14.2	0.4

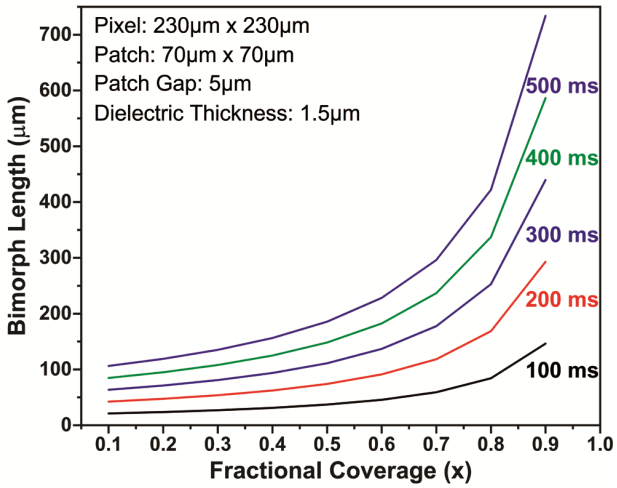

Fig. 8 — Bimorph actuator length vs Au fractional coverage

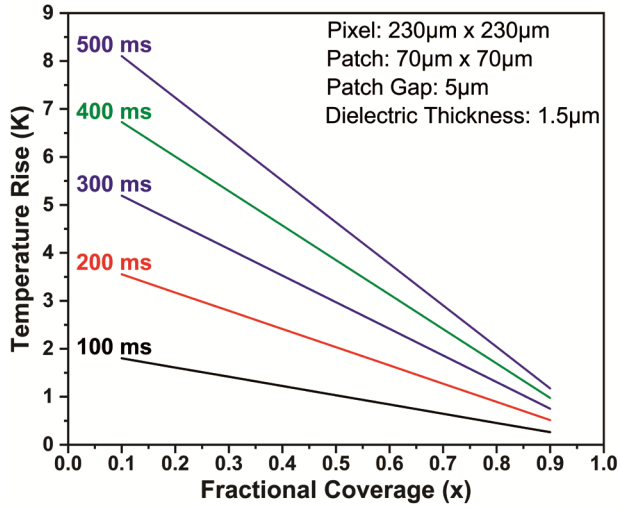

Fig. 9 — Temperature Rise vs Au fractional coverage

at 8 µm to accommodate fabrication tolerances. Increasing the fractional Au coverage raises the thermal conductance due to gold's high thermal conductivity, necessitating a longer bimorph to achieve the target conductance for a given response time. Figure 9 shows the corresponding temperature rise as a function of fractional coverage. The maximum temperature decreases with increasing Au coverage, primarily due to enhanced heat dissipation. A similar trend is observed for responsivity ($d\theta/dP$), which also decreases with increasing fractional coverage, as shown in Fig. 10.

The Au fractional coverage introduces a trade-off among response speed, detector responsivity, and the length of the bimorph actuator. Increasing the Au fractional coverage enhances thermal conductance, which supports fast response but reduces the

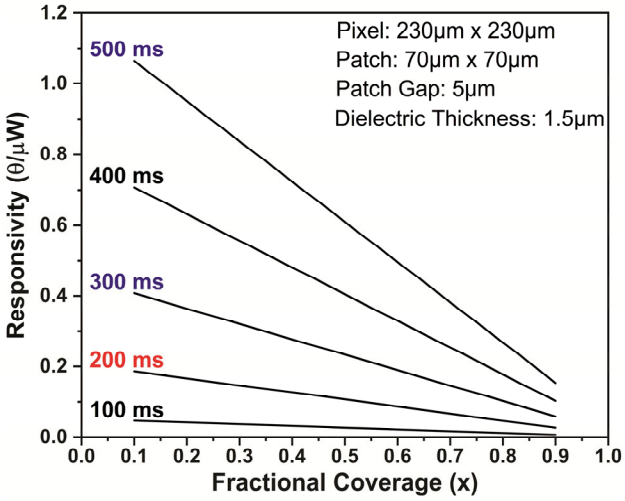

Fig. 10 — Responsivity vs Au fractional coverage

maximum temperature and, consequently, the responsivity. To maintain response speed, the bimorph length must be increased; however, longer bimorph actuators suffer from residual stresses and impose layout constraints. Conversely, reducing fractional coverage lowers thermal conductance, yielding higher temperature rise and improved responsivity, but at the expense of slow speed.

Although response times below 100 ms are desirable for high-speed THz imaging, the associated increase in thermal conductance severely limits the temperature rise, leading to negligible responsivity. To balance speed and performance while maintaining structural compliance, a response time of 300 ms with a fractional Au coverage of 0.8 is selected. For a 230 µm × 230 µm platform with a 1.5 µm dielectric thickness, the thermal capacitance is 1.75×10^{-7} JK^{-1}. Achieving τ =300 ms, therefore, requires a thermal conductance of 2.92×10^{-7} W K^{-1} per bimorph. With the width fixed at 8µm, the analytical model yields a total actuator length of 253 µm, consisting of a 202.3 µm Au–SiO_2 composite section and a 50.5 µm SiO_2 section. The optimized design predicts a temperature rise of 1.31 K, a thermomechanical sensitivity of 0.078°/K, and a responsivity of 0.08°/µW at a modulation frequency of 3 Hz. The accuracy of the analytical model and the design results is validated using finite-element analysis in the subsequent section.

2.4 Finite Element Simulation of THz Detector

Finite-element analysis of the optimized THz detector is performed in CoventorWare®, with structural dimensions shown in Fig. 11.

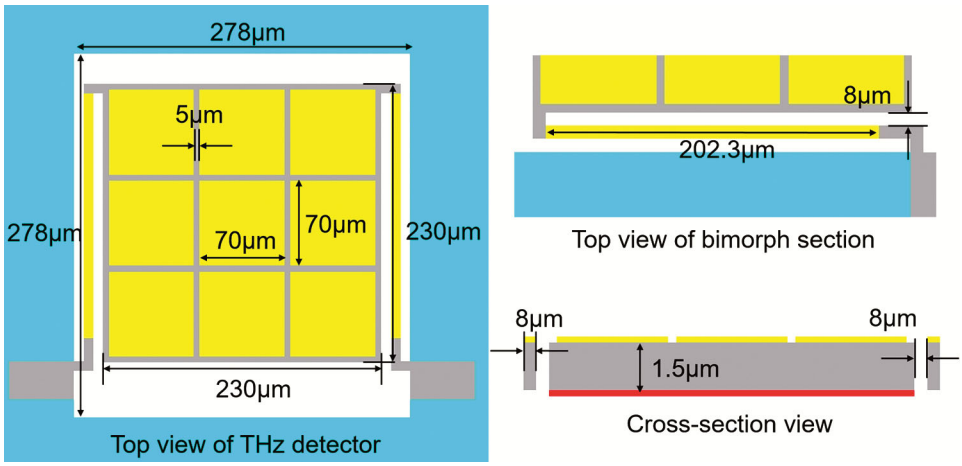

Fig. 11— Layout of the optimized THz detector

A tetrahedron parabolic mesh with a minimum element size of 0.5µm is used in the regions expected to exhibit high stresses, such as the bimorph actuators. A coarser mesh with a minimum element size of 5µm is used in the central platform to reduce the simulation time. Successive global refinements verified the mesh convergence until the temperature and deflection results are reproducible. The thermomechanical sensitivity is determined by sweeping the detector bottom temperature from 295 to 303 K and measuring the resulting platform angular deflection. Curve fitting of the simulated response (Fig. 12) yields a sensitivity of 0.063°/K, in good agreement with the analytically predicted value of 0.078°/K.The detector responsivity is subsequently evaluated by applying a uniform heat flux corresponding to incident THz powers ranging from 1 µW to 10 µW to the metamaterial absorber, while maintaining the detector bottom surface at 295 K to emulate an ideal heat-sink boundary condition. The simulated deflection of the suspended platform as a function of incident power is presented in Fig. 13. From the fitted response curve, a responsivity of 0.056°/µW is extracted, which is in reasonable agreement with the analytically calculated value of 0.08°/µW.

The steady-state thermal distribution of the THz detector with an incident power of 1 µW is shown in Fig. 14. The results indicate that heat is primarily confined to the suspended platform region, resulting in a temperature rise of 1.25 K, which is in close agreement with the analytically predicted value of 1.31 K.

Beyond thermally induced actuation, residual stresses within the constituent layers substantially affect the post-release deflection of the bimorph

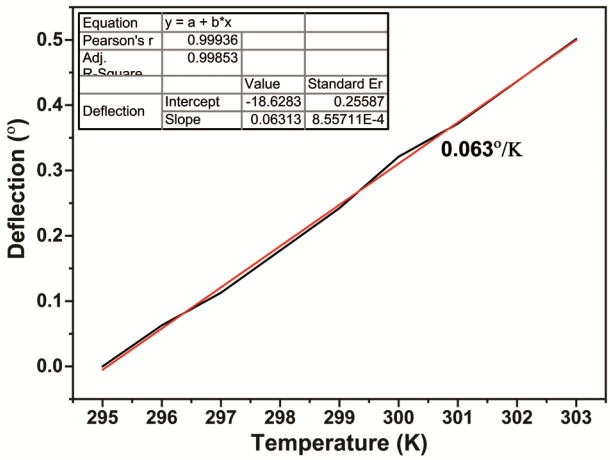

Fig. 12— Platform deflection vs temperature

actuator[28]. To quantify this effect, the intrinsic stress values are taken from the literature[28], and a biaxial tensile stress of 24 MPa is applied to the gold, while a compressive stress of 300 MPa is applied to the SiO_2 layer. The simulation predicts a post-release angular tilt of 17.12° for the suspended platform (Fig. 15), which is used as an offset to calculate the thermomechanical sensitivity and responsivity in Figs. 12 and 13, respectively. Estimating stress-related effects is critical to ensure accurate predictions of actuator behaviour and reliable implementation in deflection-based sensing systems[29].

The overall consistency between simulation and analytical results validates the accuracy of the analytical method. The optimized design is proposed to be fabricated using a combination of surface and bulk micromachining consisting of following steps (a) Thermal growth of 1µm thick SiO_2 on a silicon substrate, (b) Sputter deposition and patterning of the

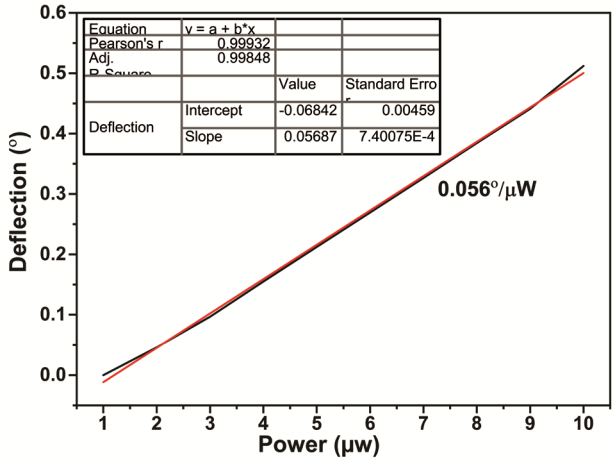

Fig. 13 — Platform deflection vs incident power

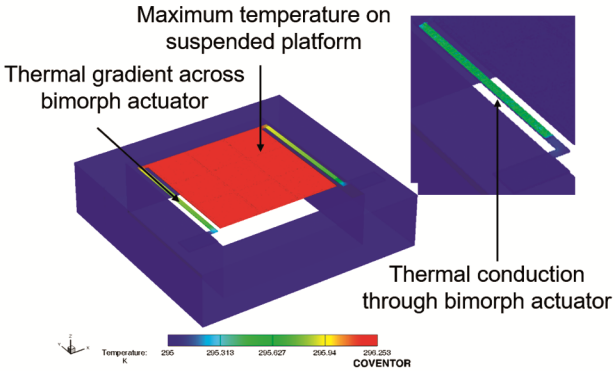

Fig. 14 — Steady-state thermal distribution across the detector

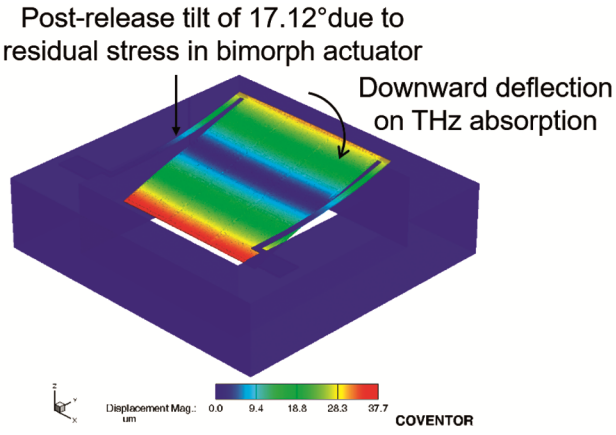

Fig. 15— Stress-induced post-release tilt of suspended platform

bottom Au ground layer, (c) PECVD deposition of 1.5 μm thick SiO_2 layer, (d) Patterning of SiO_2 layer forming the bottom layer of bimorph actuator and dielectric absorber, (e) Sputter deposition and patterning of the top Au layer forming upper layer of bimorph actuator and metamaterial patches, and (f) Platform release using backside Deep Reactive Ion Etching (DRIE). While residual stress in the Au and SiO_2 layers can be achieved through controlled deposition and post-deposition annealing, typical lithographic tolerances (±1–2 μm) would introduce less than 5-10 % variation in the device performance. The noise performance of the optimized THz detector is discussed in the subsequent section.

2.5 NEP Calculation of THz Detector

Noise mechanisms play a critical role in determining the ultimate sensitivity of terahertz (THz) detectors and must therefore be carefully evaluated. In thermal THz detectors, the fundamental noise limit is typically governed by temperature-fluctuation noise (N_{TF}), which originates from stochastic microscopic heat exchange between the detector and its thermal surroundings. In the proposed bimorph actuator–based architecture, such temperature fluctuations induce random variations in the actuator temperature, leading to mechanical displacement noise and spontaneous platform oscillations. In addition to N_{TF}, thermomechanical noise (N_{TM}) arises from Brownian motion of the mechanically compliant structure and is determined by the effective stiffness, damping characteristics, and resonant frequency of the bimorph actuator. Background fluctuation noise (N_{BF}), primarily associated with radiation exchange, is negligible under vacuum operation and controlled laboratory conditions. Consequently, the overall noise performance of the detector is predominantly governed by the combined contributions of N_{TF} and N_{TM}, and given by[26]

$$N_{TF} = \frac{RT\sqrt{4K_B GB}}{\eta} \quad \ldots(20)$$

$$N_{TM} = \frac{360}{\pi L_{leg}}\sqrt{\frac{4K_B GB}{Qk\omega_o}} \quad \ldots(21)$$

where K_B is the Boltzmann constant, B is the electronic bandwidth taken as unity, and T is the absolute temperature. k is the structural stiffness, and ω_o is the resonant frequency of the structure, which are calculated using a finite element simulation and found to be 0.11 N/m and 5.49 kHz, respectively. Q is the quality factor of the structure, which is approximately 1000 under vacuum conditions[30]. The total noise of the detector is the Root Mean Square (RMS) of two noise components and is given by[22]

Table 2 — A comparison of different bimorph-based THz detectors

Frequency Range	Pixel Size	Bimorph Layer	Absorption	Response Time	Responsivity	NEP
3.8 THz[26]	200 μm×200 μm	Al-SiO_x	95 %	300 ms	0.2°/μW	45 nW
0.5-2 THz[18]	200 μm×200 μm	Parylene-Ti	40 %	-	192 nm/K	40.4 pW
3.24-3.98 THz[22]	185 μm×185 μm	Au-Si_3N_4	90 %	100 ms	24.8 μm/μW	38.2 pW
1 THz[31]	200 μm×200 μm	Al-SiO_2	>90 %	1400 ms	396 nm/K	-
693 GHz[32]	51 μm×49 μm	Au-SiN_x	40 %	10 ms	-	29.6 nW
1 THz (Current work)	230 μm×230 μm	Au-SiO_2	>85 %	300 ms	0.056°/μW	2 pW

$$N_{Total} = \sqrt{N_{TF}^2 + N_{TM}^2} \quad \ldots(22)$$

At an operating temperature of 295 K and under vacuum operation, the temperature-fluctuation noise (0.17 μdeg) significantly exceeds the thermomechanical noise (4.8×10^{-15} deg), confirming that N_{TF} is the dominant noise source while N_{TM} is negligible. The noise-equivalent power (NEP), defined as the minimum detectable incident power for a unit signal-to-noise ratio in a 1 Hz bandwidth, is obtained as the ratio of the total output noise to the detector responsivity and is given by[22]

$$NEP = \frac{N_{Total}}{R} \quad \ldots(23)$$

The detector exhibits an NEP of 2 pW at a responsivity of 0.080°/μW under vacuum conditions at room temperature. In non-vacuum conditions, natural convection would increase the thermal conductance and NEP, as N_{TF} scales with the square root of thermal conductance. Therefore, while operating at ambient pressure might result in faster response, vacuum operation is preferred to achieve high sensitivity and a low NEP in imaging applications.

3 Results

The optimized metamaterial absorber exhibits polarization-insensitive absorption exceeding 80 % at 1 THz, with stable performance over incidence angles up to 45°, ensuring efficient THz-to-thermal energy conversion. The developed analytical model establishes relationships among thermal capacitance, thermal conductance, responsivity, and response time, enabling systematic optimization of the detector and Au–SiO_2 bimorph structure. The optimization approach results in a platform with dimensions of 230 μm × 230 μm, a 1.5 μm dielectric thickness, and 0.8 fractional Au coverage, yielding a designed time constant of 300 ms with a bimorph length of 253 μm. Finite-element simulations validate the analytical predictions, showing a thermomechanical sensitivity of 0.063°/K and a responsivity of 0.056°/μW. The simulated temperature rise of ~1.25 K for 1 μW incident power closely matches the analytical estimate. Noise analysis indicates that temperature-fluctuation noise dominates thermomechanical noise, yielding a noise-equivalent power (NEP) of approximately 2 pW at 295 K under vacuum conditions. The resulting detector performance is comparable to or better than previously reported bimorph-based THz detectors, as shown in Table 2.

4 Conclusion

This work presents the design and optimization of a metamaterial-enhanced MEMS-based THz detector for room-temperature imaging through a coupled analytical and finite-element approach. The developed analytical model successfully captures the relationships among thermal, mechanical, and electromagnetic parameters, enabling systematic optimization of detector performance. By introducing fractional Au coverage as a key design parameter, the study establishes an effective mechanism to balance the sensitivity–speed trade-off. The analytical and finite element simulation results are in close agreement, validating the robustness of the proposed design methodology. This level of sensitivity, combined with moderate response time and scalable design parameters, positions the proposed detector as a strong candidate for practical THz imaging systems. Overall, the presented design approach can be readily extended to other frequency bands through appropriate geometric scaling of the metamaterial absorber and optimization of the thermo-mechanical structure, thereby supporting the advancement of compact, low-cost, and high-sensitivity THz detectors.

Acknowledgment

The authors acknowledge the financial support under the Project Code-MMP015201 under the DELTA Mission, funded by Council of Scientific and Industrial Research, India.

References

1 Kim S M, Hatami F, Harris J S, Kurian A W, Ford J, King D, Scalari G, Giovannini M, Hoyler N, Faist J, Harris G, *Appl Phys Lett*, 88 (15) (2006) 153903.

2 Federici J F, Schulkin B, Huang F, Gary D, Barat R, Oliveira F, Zimdars D, 20 (7) (2005) S266.

3 Gowen A A, O'Sullivan C, O'Donnell C P, *Trends Food Sci Technol*, *25* (1) (2012) 40.

4 Otsuji T, *IEEE Trans Terahertz Sci Technol*, 5 (6) (2015) 1110.

5 Sizov F, *Semicond Sci Technol*, , 33 (12) (2018) 123001.

6 Rogalski A & Sizov F, *Opto-Electron Rev*, 19 (3) (2011) 346.

7 Bielecki Z, Mikolajczyk J, Wojtas J, *Sensors*, 24 (21) (2024) 6784.

8 Oda N, Kurashina S, Miyoshi M, Doi K, Ishi T, Sudou T, Morimoto T, Goto H, Sasaki T, *39th International Conference on Infrared, Millimeter, and Terahertz waves (IRMMW-THz)*, IEEE, Tucson, AZ, USA, 2014 pp. 1–2.

9 Oda N, Sano M, Sonoda K, Yoneyama H, Kurashina S, Miyoshi M, Sasaki T, Hosako I, Sekine N, Sudou T & Ohkubo S, *Infrared Technol Appl XXXVII*, (2011**)** 80121B.

10 Hao D, Liu J, Zou P, Zhang Y, Moro R & Ma L, *Laser Photon Rev*, 18 (9) (2024) 2301210.

11 Jiang Z, Leng J, Li J, Li J, Li B, Yang M, Wang X & Shi Q, *Photon*, *10* (6) (2023) 621.

12 Shen X, Cui T J, Zhao J, Ma H F, Jiang W X & Li H, *Opt Express*, 19 (10) (2011) 9401.

13 Tao H, Landy N I, Bingham C M, Zhang X, Averitt R D & Padilla W J, *Opt Express*, 16 (10) (2008) 7181.

14 Huang L, Chowdhury D R, Ramani S, Reiten M T, Luo S-N, Taylor A J & Chen H-T, *Opt Lett*, 37 (2) (2012) 154.

15 Li C, Zhang Y & Hirakawa K, *Sensors*, 23 (13) (2023) 5938.

16 Zhou H, Yang C, Hu D, Li D, Hui X, Zhang F, Chen M & Mu X, *Appl Phys Lett*, 115 (14) (2019) 143507.

17 Liu Z, Guo L & Zhang Q, *Nanomater*, 9 (10) (2019) 1351.

18 Bilgin H, Zahertar S, Sadeghzadeh S, Yalcinkaya A D & Torun H, *Sens Actuators Phys*, 244 (2016) 292.

19 Bilgin H, Yalcinkaya A D & Torun H, *Procedia Eng*, 120 (2015) 15.

20 Li K, Liang Y, Liu Y & Lin Y-S, *Microsyst Nanoeng*, 11 (1) (2025) 2.

21 Wen Y, Jia D, Ma W, Feng Y, Liu M, Dong L, Zhao Y & Yu X, *Microsyst Nanoeng*, 3 (1) (2017) 17071.

22 Zhu H, Wang K, Liu G, Wang G, Mou J, Zhang W & Wei G, *Micromachine*, 13 (5) (2022) 805.

23 Grbovic D, Karunasiri G & Alves F, *Terahertz, RF, Millimeter, Submillimeter-Wave Technol Appl XI*, San Francisco, United States, 2018 p. 37.

24 Bansal D, Kumar A, Kumar P, Kaur M & Rangra K, *Prog Electromagn Res M*, 38 (2014)123.

25 Kearney B, Alves F, Grbovic D & Karunasiri G, *Opt Mater Express*, 3 (8) (2013) 1020.

26 Alves F, Grbovic D, Kearney B, Lavrik N V & Karunasiri G, *Opt Express*, 21 (11) (2013) 13256.

27 Sellier A, Teperik T V & De Lustrac A, *Opt Express*, 21 (S6) (2013) A997.

28 Kumar A, Ashudeep, Bansal D, Kumar P, Anuroop, Khushbu & Rangra K, *Microelectron Eng*, 221 (2020) 111192.

29 Alves F, Grbovic D, Arruda J, Santos R & Karunasiri G, *8th International Congress on Advanced Electromagnetic Materials in Microwaves and Optics*; IEEE Denmark, 2014 pp. 10–12.

30 Datskos P G, Lavrik N V & Rajic S, *Rev Sci Instrum*, 75 (4) (2004) 1134.

31 Grbovic D & Karunasiri G, Fabrication of Bi-Material MEMS Detector Arrays for THz Imaging, Eds, Orlando, Florida, USA, 2009 p. 731108.

32 Tao H, Kadlec E A, Strikwerda A C, Fan K, Padilla W J, Averitt R D, Shaner E A & Zhang X, *Opt Express*, 19 (22) (2011) 21620.